ROYAL SOCIETY
OF CHEMISTRY

PAPER

Check for updates

View Article Online
View Journal | View Issue

Corrosion behavior and mechanism of X80 steel in silty soil under the combined effect of salt and temperature

Xiangling Bai, [a] Bin He, [*a] Pengju Han, [*a] Ruizhen Xie, [b] Funan Sun, [a] Zhiwei Chen, [a] Yuting Wang [a] and Xinyu Liu [a]

In this study, X80 pipeline steel was embedded in silty soil with different salinities and subjected to corrosion at a constant temperature for 24 h before electrochemical testing. The effect of soil medium, temperature, and salt content on the kinetics of corrosion behavior of X80 steel was analyzed. Furthermore, the compositions and structures of the corrosion products were analyzed by X-ray photoelectron spectroscopy and scanning electron microscopy. Based on the results, the anodic dissolution reaction mechanism of X80 steel in silty soil was determined, the differences in the corrosion process caused by different soil systems were comprehensively contrasted, and the impact of the migration process of heterogeneous silty soil on corrosion behavior under different conditions was systematically explored. Comparative analysis revealed that chloride ions possess strong adsorption ability at temperatures above freezing point and that more oxidized substances are present in the deposited layer on the surface of corroded steel, which facilitates the occurrence of corrosion under deposition. At temperatures below freezing point, the sulfate ions present in the pore solution contribute to crystallization-induced expansion and lead to swelling and deformation of the soil, rendering the X80 steel more prone to corrosion in sulfate corrosion environments.

1. Introduction

The global energy demand was estimated to have decreased by about 4.5% in 2020, attributed to the abrupt outbreak of the novel coronavirus disease (COVID-19) that stalled global economic activity and impacted the completion of various tasks in the energy sector of different countries. However, with a total share of 55.9%, oil and natural gas continue to occupy the largest share of the primary energy consumption structure.[1,2] Moreover, various energy policies in different countries are capable of strengthening support for the industry to mitigate the impact of the epidemic as well as to actively achieve progress by further intensifying systemic energy reforms and advancing in the construction of support systems and clean, low-carbon, efficient, and safe energy systems.[3,4]

Most recently developed oil and gas fields are present in more remote geographic locations, and cause problems in construction and support systems due to difficult service conditions. Among them, the construction and operation of oil and gas pipelines encounter harsh environmental conditions and operational requirements such as low-temperature environments, highly corrosive soil, high-pressure delivery, and

long-range transport. In order to improve the operating quality and assure the security of energy supply, pipeline steel requires higher strength and toughness.[5] Each enhancement in the pipeline steel grade results in a cost reduction of 5–15%. For this reason, currently, the API 5L X80 steel with high tensile strength is widely used in the oil and gas industry.[6–8]

The failure that occurs during the service life of pipelines can be broadly divided into the following three categories: excavation damage, material defects, and corrosion effects.[9–12] Inhomogeneous and porous soil cause relatively complex corrosion of buried pipeline steel, based on the interaction of multiple simultaneous reactions. As a result, the direct contact between the steel surface and the erosive soil environment is regarded as a significant cause of its corrosion failure.[9,13] Previously, extensive research efforts have been devoted to the study on the electrochemical corrosion reaction at the soil–steel interface,[14–17] and a more mature theory has been established. Most of the reactions correspond to oxygen-depolarized corrosion. Elementary reaction processes are as follows:

First, iron dissolves in the anode area under the loss of electrons (anodic oxidation reaction: $Fe \rightarrow Fe^{2+} + 2e^-$), and oxygen reduction occurs at the cathode (cathodic reduction reaction: $O_2 + 2H_2O + 4e^- \rightarrow 4OH^-$). Then, in acidic soil environments, iron ions enter the soil solution as hydrated iron cations ($Fe^{2+} + nH_2O \rightarrow Fe^{2+} \cdot nH_2O$), in near-neutral or alkalescent soil environments, iron ions, after entering the soil,

College of Civil Engineering, Taiyuan University of Technology, Taiyuan 030024, P. R. China. E-mail: 13834569544@163.com; hebin@tyut.edu.cn

Mechanics Institute, Jinzhong University, Jinzhong 030619, P. R. China

react with hydroxyl ions (OH^-) to form iron(II) hydroxide $Fe(OH)_2$ ($Fe^{2+} + 2OH^- \rightarrow Fe(OH)_2$). However, this hydroxide being unstable gets partly dehydrated to iron(II) oxide (FeO) and partly continues to react with the corrosion products iron(III) oxide hydroxide (FeO(OH)), iron(III) oxide (Fe_2O_3), and iron(II,III) oxide (Fe_3O_4).

Saline soil is the generic term for soil containing excessive amount of salt and/or alkaline components. Owing to the adverse effects of increasing soil salinity, soil salinization has gradually become an important global ecological and environmental problem that requires urgent research attention. Chloride and sulfate anions are major components of soil-soluble salts. Chloride contained in the soil is primarily affected by climate, terrain, and human activities, while sulfate content in the soil is mostly affected by acid rain, landform, geological, and climatic conditions.[18] Indeed, the migration, aggregation, and transformation of inorganic salts in the soil vary in different areas, and their spatial variability is large. It has been demonstrated that the permeability of chloride ions is a leading cause of corrosion of bars used in a working environment containing chloride ions, while the presence of sulfate restrains the diffusion of these ions.[19] Salt heave and frost heave deformations caused by physical or chemical reactions in the sulfate-containing soil due to temperature changes have also become a considerable and continuing hurdle for transportation security.[20] The safety and durability of buried pipeline steel under the synergistic effect of salt and temperature have rarely been explored till date. Thus, investigation of more improved studies on the differences in corrosion behavior caused by chloride ions and sulfate ions in soil pore solution and their respective corrosion mechanisms is highly desirable. The corrosion behavior of pipeline steel buried in soil under the combined influence of salt and temperature requires further and deeper exploration, and the theoretical questions involved further require systematic investigation. The corrosive nature of soil, explicitly of the external corrosion environment of buried pipelines, should be assessed in a viable way to provide basic data and a scientific basis for research on corrosion-related questions in other similar soil environments with the objective to improve the effectiveness and efficiency of corrosion-preventing engineering.

For this purpose, chloride ions and sulfate ions, which are ubiquitous in various soil environments and highly corrosive, were selected in this study to investigate the corrosion behavior of X80 steel under the synergistic effect of salt and temperature in the soil environment. Electrochemical measurements were conducted to determine the corrosion rate, and further analysis was performed to investigate the corrosion mechanism in different soil environments. The structure, morphology, and type of the corrosion products were analyzed by scanning electron microscopy (SEM), X-ray photoelectron spectroscopy (XPS), and other surface analyses techniques.

2. Experimental

2.1. Materials and sample preparation

The test soil samples were taken from the vicinity of buried oil and gas pipelines in the district of Xiaodian, Taiyuan City, Shanxi Province, China. The sampling area is schematically

outlined in Fig. 1. The sampling depth of the soil samples was 1.2 m. The soil was Quaternary sediment formed by weathering processes, and soil texture was classified as alkaline silty soil (1.8% sand, 68.9% silt, 19.3% clay). Some of the physical parameters are listed in Table 1. After retrieving the undisturbed soil, the soil samples were air-dried, mechanically crushed, passed through a soil sieve with a mesh size of 1 mm, and washed with sterile deionized water. Further, excess salt was washed away, and the soil samples were placed in a thermostatic blast drying oven at 378.15 K for at least 6 h prior to their use to ensure the complete removal of residual moisture. In the trials, sodium chloride (NaCl, analytical grade) and sodium sulfate (Na_2SO_4, analytical grade) were dissolved in deionized water and stirred evenly to obtain saline solution as a simulation of the Cl^- and SO_4^{2-}, respectively, in the soil pore solution. The use of remolded soil ensured the repeatability and comparability of the experiments.

The X80 pipeline steel with high tensile strength and used widely in the oil and gas industry, was selected as the research object of the present study, and its chemical composition is listed in Table 2. The used X80 steel met the API Spec 5L criteria, and the carbon equivalent CE_{pcm} value is below the maximum allowable value specified in the standard. The size of the X80 steel sample for the electrochemical test was 10 mm × 10 mm × 2 mm. The sample was sanded level by level with water-resistant sandpaper on the grinding/polishing machine. After polishing with 2000# sandpaper, the sample was then cleaned in an ultrasonic bath to acquire smooth surface without scratches and no residual adsorbed materials. The copper conductor was welded to the steel and sealed with epoxy resin to retain a nominal working surface area of 1 cm^2.

In order to characterize the microstructure, the surface of steel sample was prepared *via* the following steps: inlay → grinding → polishing → erosion. First, phenolic resin was used to hot mosaic the sample. After cooling, 800–3000# sandpaper was used for surface grinding, and then diamond polishing agents with a particle size of 2.5 and 0.5 μm were utilized for coarse polishing and fine polishing, respectively. Finally, the sample was etched with electrolyte solution prepared using 96 vol% alcohol and 4 vol% nitric acid for about 6 s until the surface turned from bright to off-white (the sample used to capture SEM image was etched for about 12 s). Optical micrographs were obtained using a Leica Dmi 8C metallurgical microscope (Leica Microsystems, Wetzlar, Germany). The
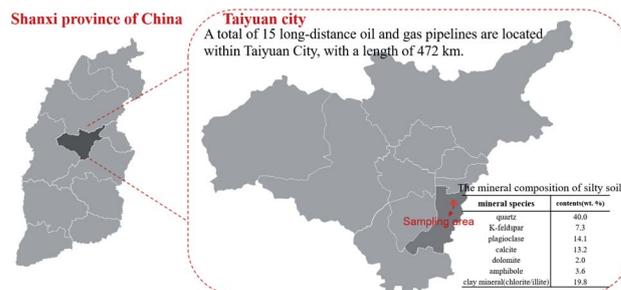

Fig. 1 The schematic illustration of the sampling area.

Table 1 Basic physical parameters of the silty soil

Parameters	Natural water content (%)	Liquid limit (%)	Plastic limit (%)	Plastic index	Specific gravity
Values	6.8	25.3	15.6	9.6	2.7

surface microstructure of X80 steel used in this experiment is shown in Fig. 2.

The optical micrographs of X80 steel surface reveal that it predominantly consists of ferrite and bainite phases. The shape of ferrite is drawn into thin strips and polygons, corresponding to acicular ferrite (AF) and polygonal ferrite (PF) morphologies. The shape of bainite is granular (GB), with fine grains and irregular distribution. Among them, GB, as a typical nonequilibrium phase, has high electrochemical activity.[21] Owing to the electrochemical inhomogeneity, the presence of tiny areas with different levels of potential in the metal surface constitutes various corrosion micro-galvanic cells. The organization with more active chemical properties and prone to be deprived of electrons in the structure of the material acts as the first place for the corrosion to occur. In the original structure of X80 steel, due to the different corrosion potentials of the phases, the alpha phase with a lower corrosion potential gets corroded as the anode, the beta phase with a higher corrosion potential is relatively preserved as the cathode, and the anode alpha phase acts as the active site of pitting corrosion. Notably, this heterogeneous inhomogeneity of metal can cause pitting-type corrosion.[22] The GB in the structure of X80 steel usually acts as the early-developing region for pitting. These locations lead to the initiation of the interfacial corrosion process when they are in contact with the corrosive environment.

The workflow of sample preparation is illustrated in Fig. 3.

2.2. Experimental setup

The dried soil sample was adequately stirred with the salt solution and then maintained in a standard constant temperature and humidity conservation box for 24 h in order to ensure the even distribution of ions in the soil pore solution. The optimal moisture content of the silty soil used in this study was calculated to be 15.30% by the standard compaction test, the maximum dry density was 1.82 g cm^{-3}, and the soil compaction coefficient was 0.90. A square insulated box with a dimension of 70.7 mm × 70.7 mm × 70.7 mm was used as a test mold, and the height of the soil sample in the mold was controlled based on the compaction coefficient.

The soil sample and steel sample were placed together in the mold box to ensure that the bottom end of the steel to be tested was 1 cm from the bottom of the mold box, and the steel working surface was in tight contact with the soil. An external thermostatic bath with an error of ±0.15 K was used as the sample temperature control setup. A temperature sensor was inserted in the middle section of the soil sample to record the soil temperature. The electrochemical test was performed after soil temperature reached the target temperature for 24 h.

2.3. Electrochemical measurements

Electrochemical measurements were performed on a CorrTest CS-350 electrochemical workstation. Electrochemical measurements were conducted using a three-electrode system with X80 steel, Pt plate electrode, and saturated calomel electrode (SCE) as the working, counter, and reference electrodes, respectively. The measurement was repeated three times, and the results of a representative experiment were obtained.

Prior to electrochemical measurements, the open circuit potential (OCP) test was first performed for the X80 steel. The sampling time was 2500 s, and the sampling frequency was 5 Hz. Impedance-frequency sweep test was performed with perturbation voltage signal of 10 mV in the frequency range from 100 kHz to 0.01 Hz with 12 data points analyzed per frequency decade. The obtained spectra were fitted by using Zview software in terms of appropriate equivalent circuits to ensure experimental precision, and the chi-square values were found to be within the required range. Before the potentiodynamic scanning test, the working electrode was stabilized by polarizing at the polarization potential for 3 min. The scanning range of the potentiometric polarization curve was −0.75 to 3 V, and the scanning rate was 1.5 mV s^{-1}.

2.4. Mass loss test

The X80 steel sample used for the weight loss method was 120 mm × 90 mm × 2 mm dimension. The sample was ground, polished, cleaned and stored in ambient conditions. The dimensions were measured by vernier caliper and the samples were weighted by analytical balance with an accuracy of 0.0001 g. The sample was embedded into epoxy resin, leaving a nominal working surface area of 120 mm × 90 mm. Soil temperature and salt content control were the same as the electrochemical test. After burying the X80 steel sample in silty soil for 24 h and removing the epoxy resin, a descaling agent (500 mL HCl + 500 mL distilled water + 3.5 g hexamethylenetetramine) was used to remove the corrosion layer. The steel sample was then cleaned in an ultrasonic bath, naturally air-dried and weighed again. Three parallel experiments were performed for each group, and the average corrosion rate (ACR) was calculated using the eqn (1).

Table 2 Chemical composition of X80 pipeline steel (wt%)

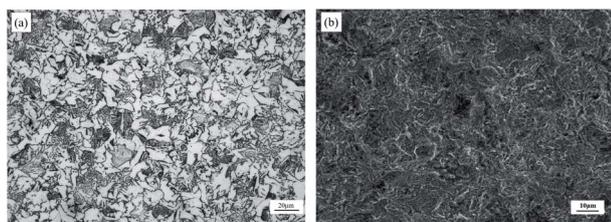| Chemical composition	Fe	C	Mn	Si	P	S	Nb	Cu	Cr	Ni	Mo	Other
Values	96.791	0.070	1.80	0.216	0.0137	0.0009	0.105	0.221	0.266	0.168	0.182	0.043

Fig. 2 Microstructure of X80 steel specimen: (a) surface optical micrographs and (b) surface SEM photomicrograph.
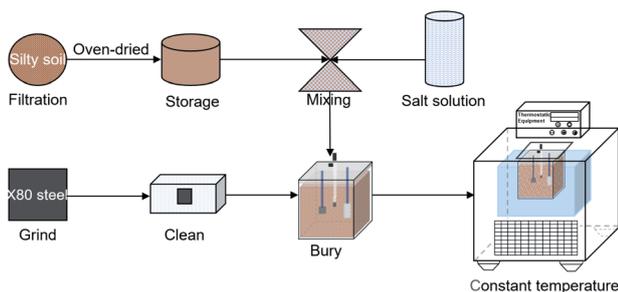

Fig. 3 The flow chart of sample preparation.

$$\text{ACR} = \frac{8.76 \times 10^4 \times W}{A \times \rho \times t} \qquad (1)$$

where ACR is the average corrosion rate (mm y^{-1}), W is the mass loss (g), A is the work area (cm^2), ρ is the steel density (7.86 g cm^{-3}) and t is the corrosion time (h).

2.5. Surface characterization techniques

The corroded working surface was slightly wiped with absolute ethanol to remove the loose soil particles attached to the surface. Then a high-magnification digital camera (Canon 6D SLR) was used to obtain the macroscopic images of surface morphology. Further, the surface morphologies of the samples were observed by all-in-one scanning electron microscopy (JSM-IT200), and surface elemental compositions were detected by energy-dispersive X-ray spectroscopy (EDS). The valence states of Fe elements were measured by an X-ray photoelectron spectrometer (XPS, Thermo Scientific K-Alpha) with the Al Kα excitation. The XPS data processing was completed by using the Avantage data software and XPSPEAK software. The 3D morphology and cross-section plot of X80 steel surface deposits were characterized using the optical profilometer (VHX-7000, Keyence).

3. Results and discussion

3.1. Corrosion behavior of X80 steel in silty soil with salt as the independent variable

3.1.1. Surface morphology and corrosion products. The surface macro–micro morphology of the X80 steel sample after corrosion in silty soil with salt concentration as the independent variable and temperature at 293.15 K is shown in Fig. 4 and

5. The macroscopic morphology indicates the formation of the Fe-oxides rust layer on the steel surface, and some amount of soil is also attached to different degrees. The sediment layer covered on the steel surface functions as protective film, which suppressed the uniform corrosion and impeded the part of reducing substances in soil to arrive at the surface.

The analysis of micro-morphology indicates that the sediment layer may be subdivided into the inner layer and the outer layer. The inner layer is thin and compact iron oxide film, with the bulk enrichment of Fe elements and a small number of O elements. The outer layer is thick but porous iron oxide film and some soil particles, with the characteristics of loose texture and scattered distribution. Moreover, defects such as pores and through-thickness cracks are observed at these sediment layers. The reduced mediator (pore water and corrosive ions) in the soil crosses the defect band, forming channels for the reduced mediator to diffuse into the steel substrate surface. As a result, the sediment layer cannot be used as a protective layer to inhibit the corrosion of the metal substrate for a long period, and this also promotes the corrosion electrochemical reaction to occur again. The porous and thin iron oxide layer (compared to the thick and compact oxide layer) would provide more routes to capture and cross more nearby corrosive ions. Noteworthy, soil is a very complicated system consisting of non-uniform three-phase system made up of solids, liquids, and gases, therefore, the occurrence of local corrosion behavior on the metal surface leads to the increase and consecutive acceleration of the reaction that could drive corrosion behavior.

Notably, the concentration of ions primarily impacts the number of pits.[23] With the increase in the ion concentration, the sediment layer on the steel surface gradually becomes denser. However, the presence of a high salt concentration leads to enhanced adsorption, which results in enlarging and spreading of the corrosion area, and it is prone to form continuous ulcer-like pits under the sediment layer. Fig. 5(a)–(c) exhibit that the rust layers formed on the surface of X80 steel in sulfate-containing silty soil are mainly grown perpendicular to the surface. Layers of loose sediments are mostly distributed in a fluffy cluster, with large quantities of cluster-like corrosion products, and the degree of erosion is relatively mild. However, in the corrosion environment of chloride-containing silty soil for the X80 steel (as shown in Fig. 4(a)–(c)), the rust layers grow along the steel surface, and the corrosion is severe.

For the area marked as red dots in Fig. 4 and 5, an EDS test was conducted to analyze the local element mapping. The results of these samples are presented in tables in each group of figures. Clearly, with increasing ion concentration, the amount of iron-dissolved corrosion products increases gradually. The elemental oxygen contents of the rust layers in the corrosive environments of chloride are higher and the iron contents are lower under 293.15 K temperature conditions. These results indicate that the elemental oxygen content is strongly influenced by the amount of soil adhesion and the content of oxide corrosion products, and it can thus be concluded that the contents of Fe oxides in the chloride-containing environment are more, and it has a stronger influence on the metal corrosion.
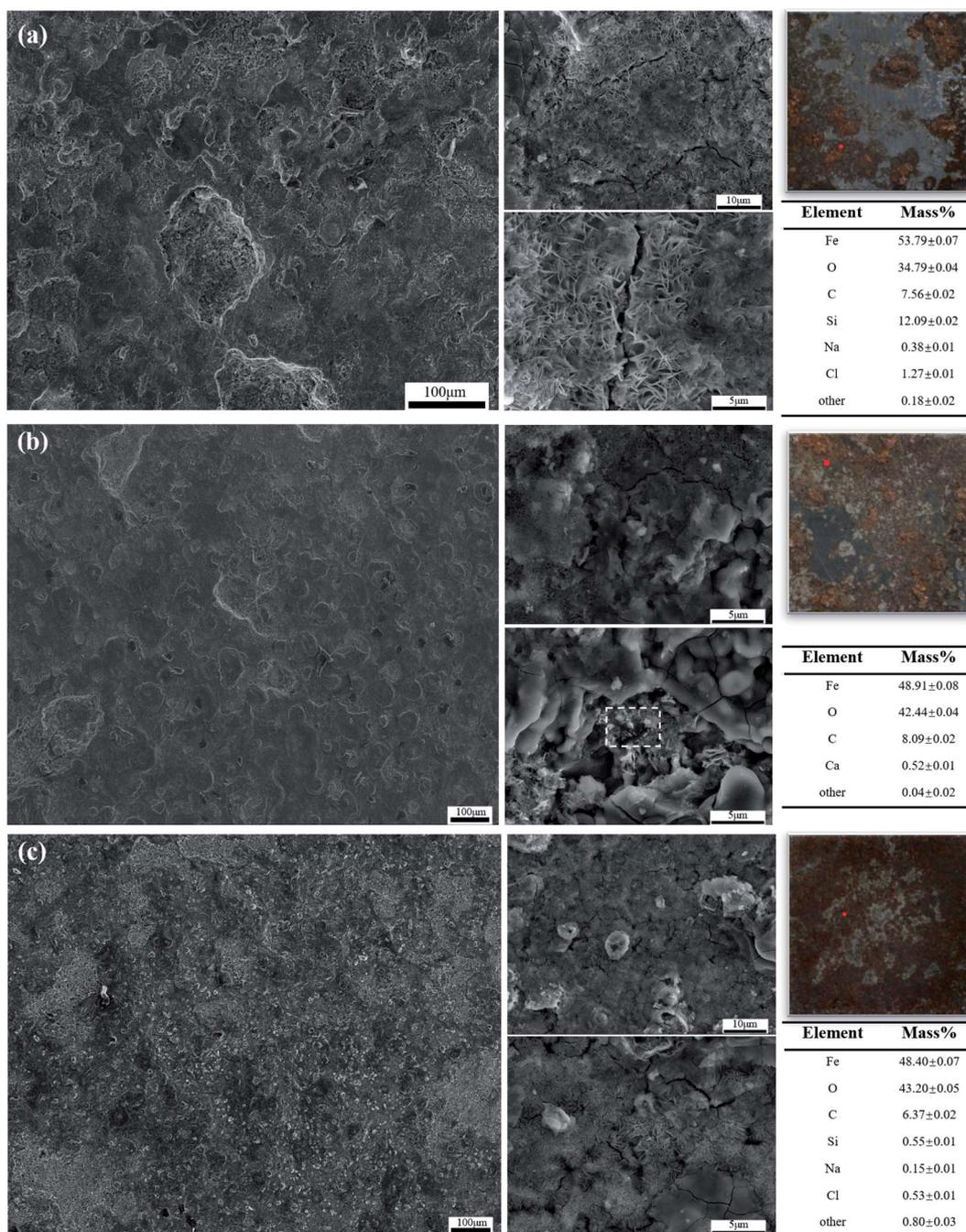
Fig. 4 X80 steel surface characterization test results in various silty media: (a)−(c) NaCl 0.3%, 1%, 2%.

EDS as a semi-quantitative method could only be used for determine the elemental content and not the specific types of compounds.[24] Therefore, it was necessary to use XPS analysis technique to further investigate the composition of the corrosion products. Notably, Fe is a transition metal element and its fine spectrum has asymmetric bimodal and satellite peaks. These peaks can be used to qualitatively and quantitatively analyze the ionic state of Fe. Thus, the Fe 2p 3/2 orbital was further analyzed by peak fitting.[11,25,26] The XPS Fe 2p 3/2 fine spectrum test and fitting results are shown in Fig. 6.

In view of the results, several conclusions can be achieved. The corrosion products formed on the X80 steel surface in various silty media were composed predominantly of Fe_2O_3, FeOOH, and Fe_3O_4, this is in accordance with the results of a few earlier studies.[27–29] Since the reduced mediator in the soil can act as the oxidant to oxidize ferrous ions to ferric ions, within various silty media, the formation and transformation processes of corrosion products on the X80 steel surface were different, and the components of the surface deposits were also different.
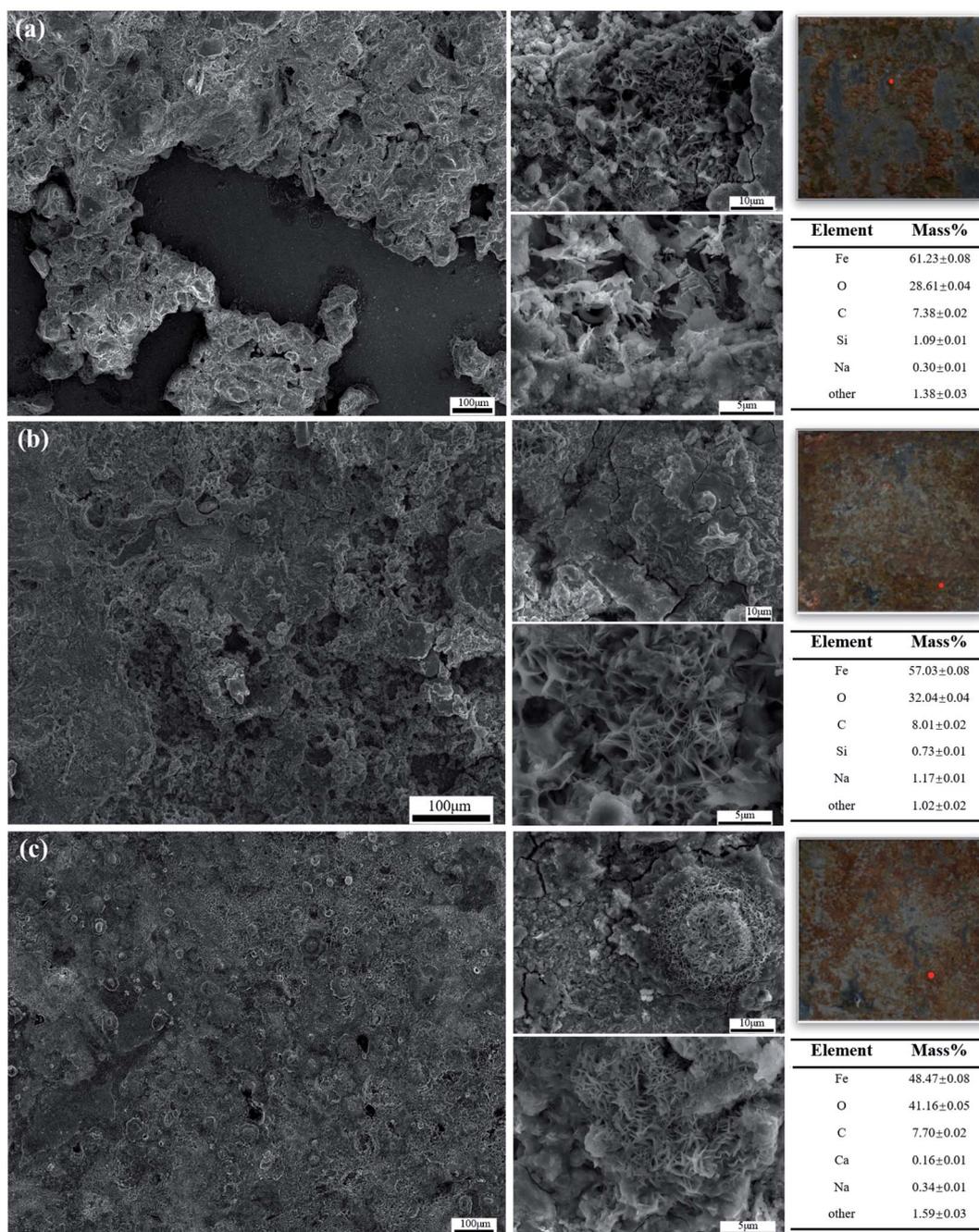
Fig. 5 X80 steel surface characterization test results in various silty media: (a)–(c) Na$_2$SO$_4$ 0.3%, 1%, 2%.

The deposited layer was composed of the products (primary products) of cathodic reaction and anodic reaction and the products (secondary products) produced due to the continued reactions of the primary products, both containing soluble and non-soluble corrosion products. FeOOH and Fe$_2$O$_3$ in the sediment have a loose and porous structure with poor protection against the metal matrix, while Fe$_3$O$_4$ is the non-soluble corrosion product with a compact structure that exhibits a better protective effect on the matrix. When the non-soluble corrosion product reaches a certain threshold, the effect of inhibiting the corrosion of the matrix increases.

In the sulfate-containing silty soil medium, with the increase in the ion concentration to 1% (as shown in Fig. 6(e)), the content of oxidation state in the X80 steel surface sediments decreases, the content of reduced state in the inner layer corrosion products increases, and soil–steel interface corrosion is suppressed. With the increase in concentration to 2% (as shown in Fig. 6(f)), the Fe$_3$O$_4$ content decreases, the content of FeOOH outer layer corrosion product increases, and the corrosion rate increases. In the chloride-containing silty soil medium (as shown in Fig. 6(a)–(c)), the Fe$_3$O$_4$ content decreases slowly with respect to an increasing ion concentration, indicating that
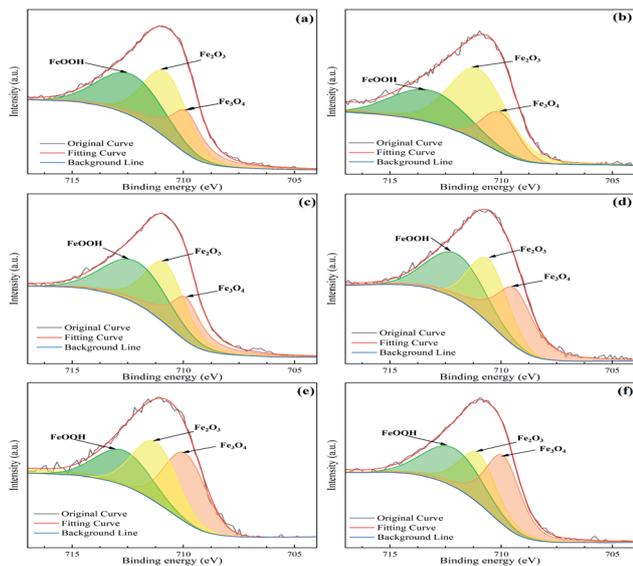
Fig. 6 High-resolution Fe 2p 3/2 XPS spectra of corrosion products on the steel surfaces: (a)–(c) NaCl 0.3%, 1%, 2% and (d)–(f) Na₂SO₄ 0.3%, 1%, 2%.

Fig. 7 High-resolution O 1s XPS spectra of corrosion products on the steel surfaces: (a)–(c) NaCl 0.3%, 1%, 2% and (d)–(f) Na₂SO₄ 0.3%, 1%, 2%.

the interface exhibits the absence of sufficient amount of oxygen supply to further continue the reaction and the corrosion products content of complete oxidation decreases. The incomplete oxidation of corrosion products due to reduced oxygen content leads to promoting the occurrence of corrosion under deposition and the onset of pitting.

Fig. 7 shows the XPS spectra of O 1s. It can be seen that the O 1s spectrum of surface deposits exhibited three peaks at 530.0 eV (metal oxides), 531.8 eV (hydroxides) and 532.9 eV (soil particles).[30,31] Different soil environments could affect working surface deposits not only composition but also morphology. In the sulfate-containing silty soil, with the increase in the ion concentration to 1% (as shown in Fig. 7(e)), there are more soil particles in surface deposits, which would show some hindrance effects and inhibit the soil–steel interface corrosion. With the increase in concentration to 2% (as shown in Fig. 7(f)), the Fe-oxides in surface deposits and corrosion kinetics behavior increases. In the chloride-containing silty soil, with the increase of ion concentration, the content of soil particles in the surface deposits decreases, whereas the content of corrosion products increases, and the corrosion rate increases.

The fitting results of the XPS spectrum of the corrosion surface deposits O 1s and Fe 2p are consistent with the corrosion morphology characterization.

To better reflect the information of the corrosion deposits on the X80 steel surface and further analyze the thickness and coverage of the deposits, the 3D morphology and cross-section plot of surface deposits is supplemented. The optical profilometry technique was found to be an efficient way for characterizing the structure and microtopography of the sample surface. It could provide qualitative images at the microscale level and further evaluate the degree of corrosion surface
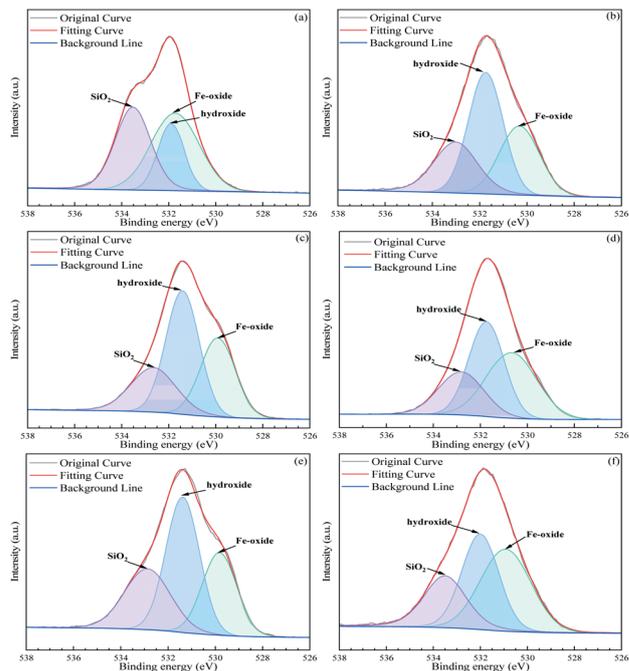
coverage.[32] The results of measurements are shown in Fig. 8 and 9.

The 3D morphology clearly shows that the corrosion deposits are of double-layer structures. In the silty soil environment with low ion concentration (as shown in Fig. 8(a)), a clear boundary line can be observed for the dense inner and loose outer layers of the X80 steel surface corrosion deposits. Still, the boundary line gradually becomes blurred with the increasing ion concentration (as shown in Fig. 8(c)). Fig. 9(a)–(c) exhibit that the corrosion deposits on the surface of X80 steel in sulfate-containing silty soil are relatively thin and flat. With the increase in ion concentration, the area covered by corrosion deposits first decreases and then increases.

However, in the corrosion environment of chloride-containing silty soil for the X80 steel, the relatively deep corrosion pits on the X80 steel surface can be observed. As the ion concentration increases, the thickness of the corrosion product becomes thicker, the degree of pitting corrosion becomes more serious, and the corrosion region becomes larger. As a result, it can be thus inferred that the chloride-containing silty soil environment is more corrosive. The 3D morphology and cross-section plot of the corrosion deposits reflect that the corrosion degree of X80 steel in different soil environments is consistent with the corresponding SEM observations.

3.1.2. Electrochemical characterization. Fig. 10 presents the OCP monitoring process for X80 steel in silty soil with salt concentration as the independent variable and temperature at 293.15 K. The thermodynamic stability information of the working electrode surface in different corrosive environments
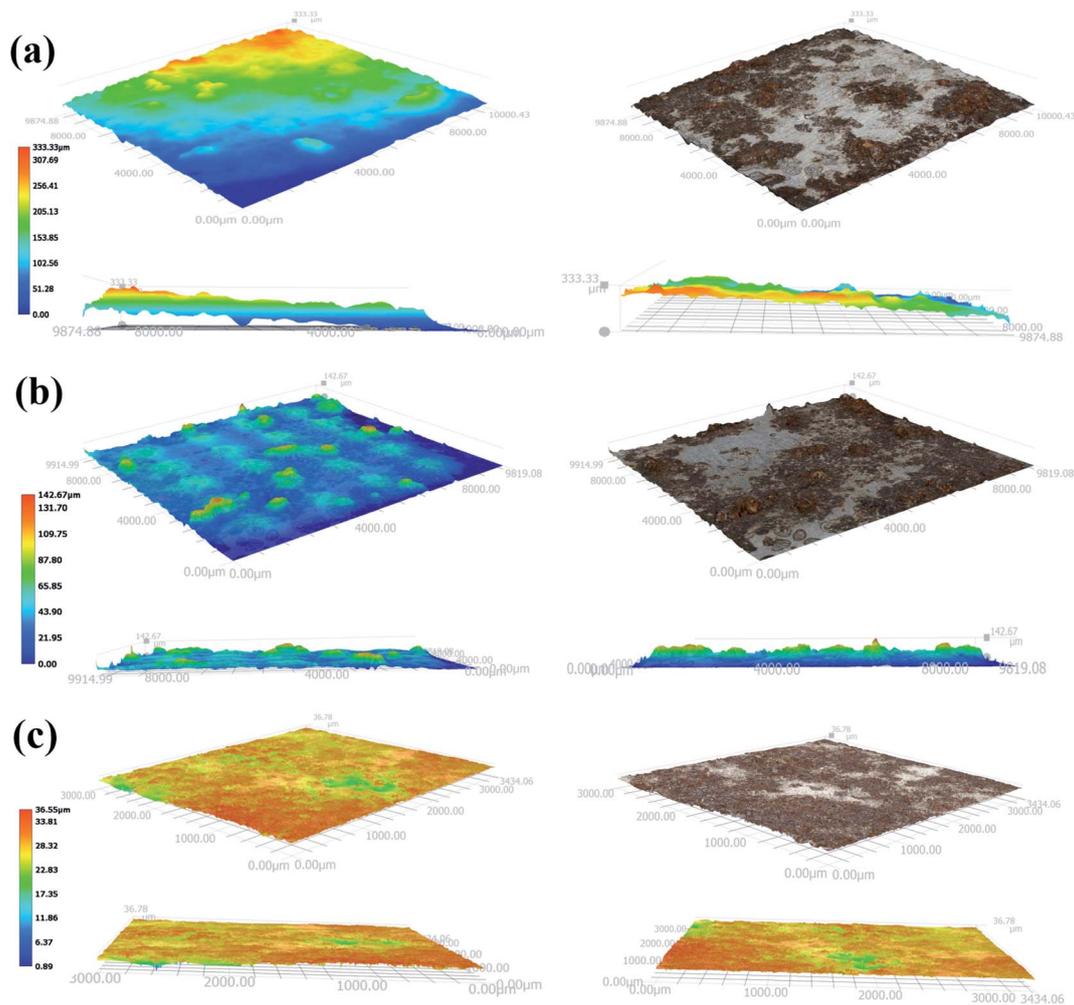
Fig. 8 3D topographical images of X80 steel surface in various silty media: (a)–(c) NaCl 0.3%, 1%, 2%.

could be reflected by the OCP value. By the OCP monitoring results, it can be observed that the silty soil corrosion system is in aerobic conditions.[39] The OCP value of the test system fluctuates slightly and tends to a stable value over time, and the OCP value of the chloride-containing environment increases as the salt content increases, whereas the value of the sulfate-containing environment first decreases and then increases. It is obvious that the former is larger than the latter. The increase of the OCP value would reflect, to a certain extent, the cathode current increases, the anode reaction promotes accordingly, and the surface electrochemical reaction in the electrode accelerates.

The polarization curves of the X80 steel in silty soil with salt concentration as the independent variable and temperature at 293.15 K are shown in Fig. 11. Evidently, when the X80 steel is present in a corrosive soil environment with chloride ion concentration of 2%, the current density maintains a low value when the measured potential is above the self-corrosion potential. When the potential reaches $-0.39E$, a significant increase of current is observed. The polarization curves of the steel in the remaining salty soil environment were observed in

the passivation region, indicating that the passivation film on partial anode domains of the steel surface prevented it from continuing active dissolution. Of course, it is not that the higher the ion concentration of the soil electrolyte, the greater the possibility of metal passivation. In contrast, the higher salt content of the soil makes it easier to damage the passivation film, thus promoting local corrosion.

In the corrosive soil environment, with a range of concentrations used in this study, the passive current densities increase with the chloride ion concentration. Moreover, the passive current densities remain almost the same with the increase of sulfate concentration. The passive current density is relatively large, indicating a large corrosion rate and it is more vulnerable to the effect of the reduced mediators in the electrolyte. Accordingly, it can be thus inferred that the chloride-containing silty soil environment is more corrosive.

The corrosion current density (i_{corr}) and corrosion potential (E_{corr}) values (as shown in Fig. 12(a) and (b)) were derived from the extrapolation of the linear portion of the anodic and cathodic branches of the measured polarization curves shown. Clear trends can be observed, that is, with the increase in the
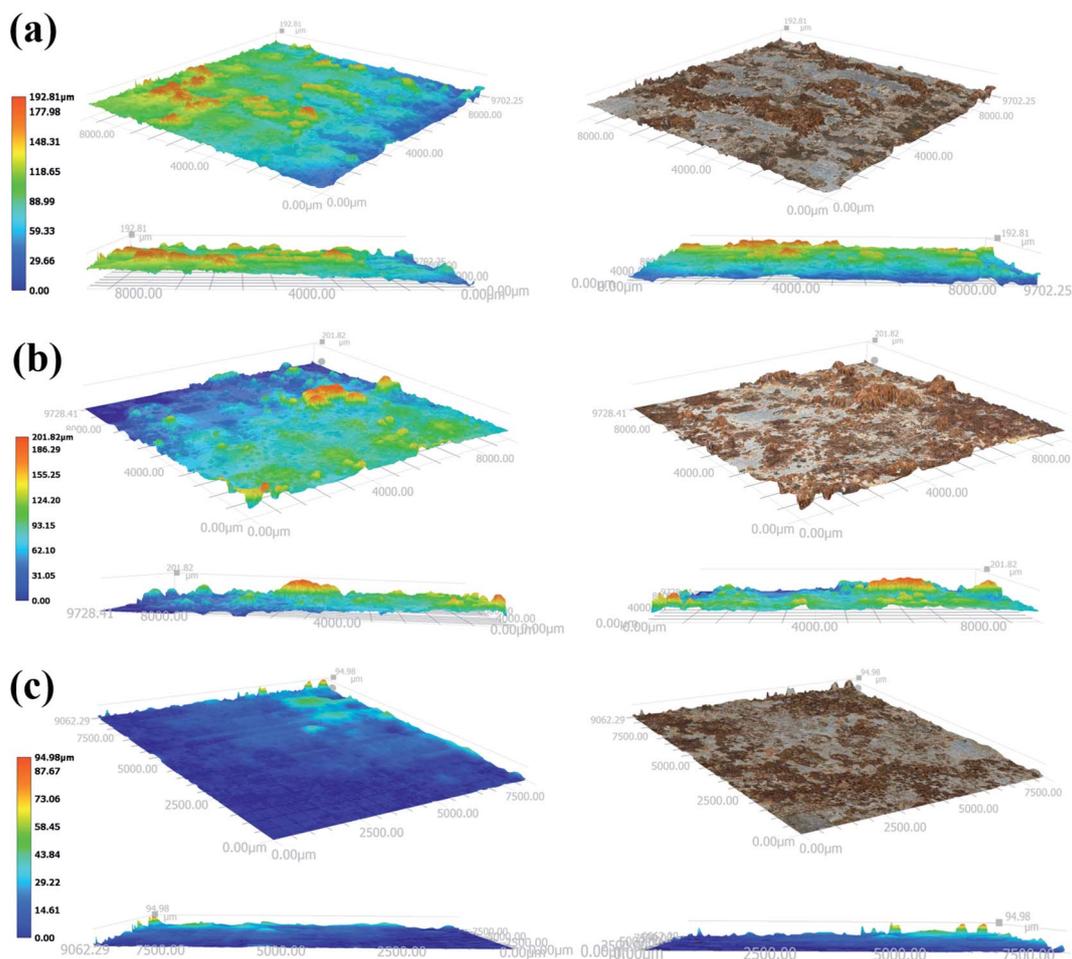
Fig. 9 3D topographical images of X80 steel surface in various silty media: (a)–(c) Na$_2$SO$_4$ 0.3%, 1%, 2%.

ion concentration, the polarization curve shifts to the high current direction and the E_{corr} of the chloride-containing soil environment also increases; however, the i_{corr} of the sulfate-containing soil environment first decreases and then increases. The potential shifts positively, which reveals that the deposits formed on the steel surface under the chloride-containing soil gradually grow thicker and denser. Nonetheless, in the sulfate-containing soil, the i_{corr} decreases. This situation indicates that the corrosion deposits formed on the steel surface at sulfate-containing soil with the concentration of 1% exhibit some inhibitory effect on the cathodic hydrogen evolution reaction and the anodic dissolution reaction. The
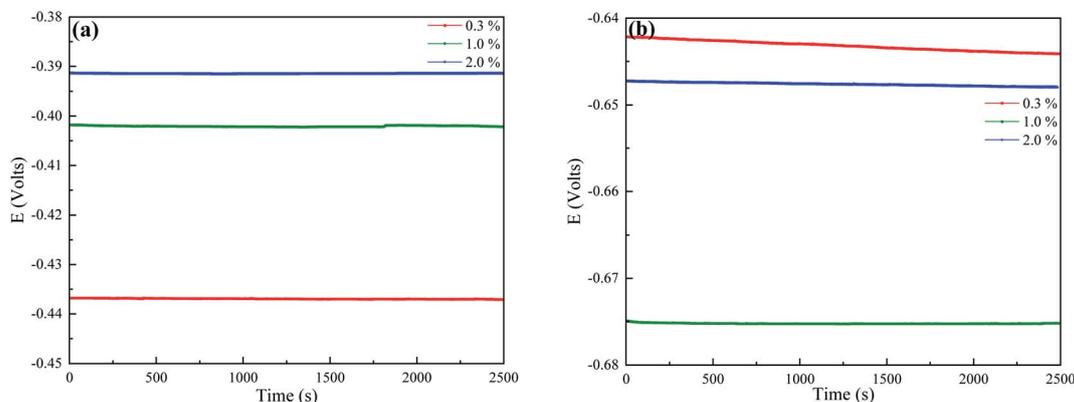

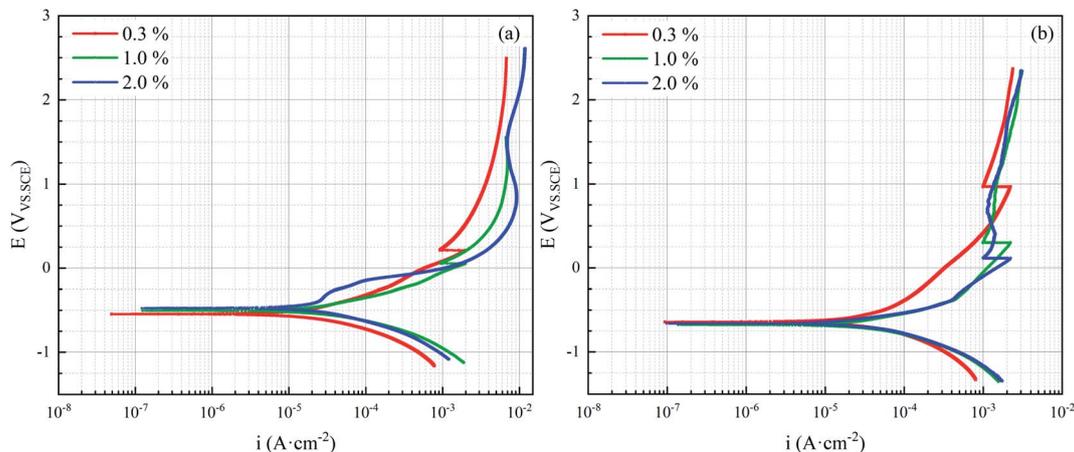**Fig. 10** Open circuit potential curves of X80 steel in various silty media: (a) NaCl and (b) Na$_2$SO$_4$.

Fig. 11 Polarization curves of X80 steel in various silty media: (a) NaCl and (b) Na$_2$SO$_4$.

corrosion rate was calculated based on Faraday's law (eqn (2)),[24] and the corresponding results are shown in Fig. 12(c). The variation tendency of corrosion rate was the same as that of i_{corr}, and the corrosiveness of chloride-containing silty soil was significantly higher than that of sulfate-containing silty soil.

$$CR = \frac{365 \times 24 \times 3600 \times M}{z \times F \times \rho \times A} \times i_{corr} \times 10 \quad (2)$$

where CR is the corrosion rate (mm y^{-1}), i_{corr} is the corrosion current density (A cm^{-2}), M is the molar mass (g mol^{-1}), z is the number of per atom-transferred electrons, F is the Faraday constant (96 485 C mol^{-1}), ρ is the steel density (7.86 g cm^{-3}), and A is the work area (cm^2).

Equivalent weight (EW) is typically considered to be the mass of metal in grams that is oxidized by the passage of one Faraday of electric charge. For alloy, the EW value is calculated by using eqn (3) as follows:[33]

$$EW = \frac{1}{\sum \frac{n_i f_i}{W_i}} \quad (3)$$

where n_i is the valence of the ith element of the alloy, f_i is the mass fraction of the ith element of the alloy, and W_i is the atomic weight of the alloy. The EW value of X80 steel used was 27.92.

For the penetration rate (PR) and mass loss rate (MR) of the steel, the calculations can be further conducted with the EW value (eqn (4) and (5)), where the value of i_{corr} can be calculated by using the Stern–Geary equation (eqn (6) and (7)).[34,35]

$$PR = 3.27 \times 10^{-3} \times \frac{i_{corr}}{\rho} EW \quad (4)$$

$$MR = 8.954 \times 10^{-3} \times i_{corr} EW \quad (5)$$

$$i_{corr} = \frac{B}{R_p A} \quad (6)$$

$$B = \frac{b_a b_c}{2.303(b_a + b_c)} \quad (7)$$

where B is the Stern–Geary coefficient, R_p is the polarization resistance, and b_a, b_c are the slopes of the anodic and cathodic Tafel reaction, respectively.

The working electrode has different relaxation times for the applied signal. Therefore, the electrochemical parameters related to corrosion of the electrode can be calculated from different frequency bands. Thus, the R_p value can be calculated from the EIS measurement for the working electrode, the i_{corr} value can be estimated from the impedance data analysis, and the mechanism of soil–steel interface corrosion can be monitored by the impedance patterns of the different shapes. The correlation corrosion rate values concluded from multiple
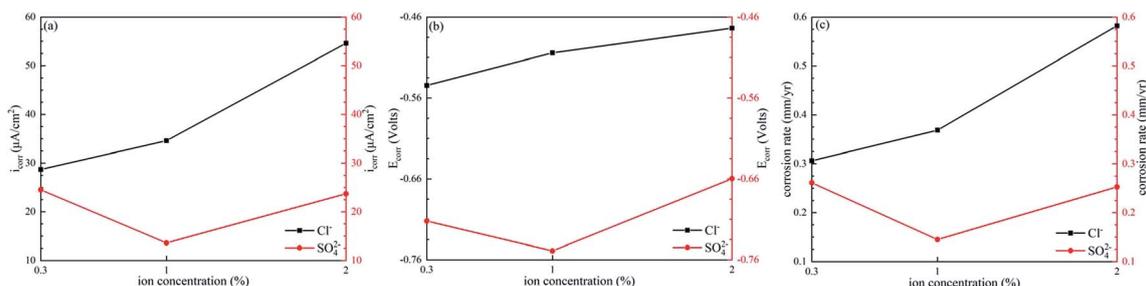

Fig. 12 Polarization curve fitting parameter value: (a) i_{corr}, (b) E_{corr}, and (c) corrosion rate.

approaches can be thus contrasted to make the result more plausible and reduce the error.[36] The EIS results of the X80 steel sample in silty soil with salt concentration as the independent variable and temperature at 293.15 K are shown in Fig. 13.

In general, R_p can be calculated via two methods by exploiting impedance spectroscopy.[36] The first method is based on the impedance modulus value. This is based on the fact that the low-frequency region in EIS reflects the Faraday process, therefore, the low-frequency impedance magnitudes can be used to characterize the electrochemical kinetic parameters of the corrosion process (i.e., $R_p = |Z|_{0.01 \text{ Hz}}$). The second method uses the $R(Q(R(QR)))$ equivalent circuit (inset of Fig. 13) fitted in the limited frequency range of the impedance spectrum: 10 000–0.01 Hz. The fitting curves are shown in Fig. 13 (black solid curve). The result approves that the χ^2 meets the requirements and has a high accuracy rate and small deviation. The R_p value is the sum of the resistance values of partial circuit components (i.e., $R_p = R_1 + R_2$). In order to exclude the effect of the semicircle portion in high-frequency region, which is mainly affected by corrosion products and salt ion penetrating the corrosion product cracks, the fit range did not include the high-frequency region of 10^5–10^4 Hz. According to the above-

mentioned method, the calculated values of R_p are listed in Table 3. By using the above-stated formulas (eqn (4)–(7)), values of PR and MR were further calculated and listed in Table 4.

According to the information extracted from the EIS results, the values of PR and CR calculated by both methods are almost same, indicating that the two calculation methods are relatively reasonable. Moreover, their variation tendency is the same as that of the corrosion rate calculated according to the polarization curve displayed above. This proves that when using electrochemical measurements to study the corrosion kinetic behavior of steel in a corrosive soil environment, the polarization curve and impedance spectroscopy can be overall considered. With the increase in the ion concentration, the radii of the semicircular arcs in the Nyquist plot decrease, the reaction resistance decreases, and the corrosion rate as well as corrosion get enhanced. The presence of chloride ions could increase the conductivity of the soil electrolyte, and the R_s value related to soil is relatively low in the chloride-containing silty soil.

With soil temperature increasing, the cathodic hydrogen evolution and anodic iron dissolution reaction simultaneously accelerated. However, the corrosion kinetics of metal is not increased with the soil temperature; rather, it is strongly
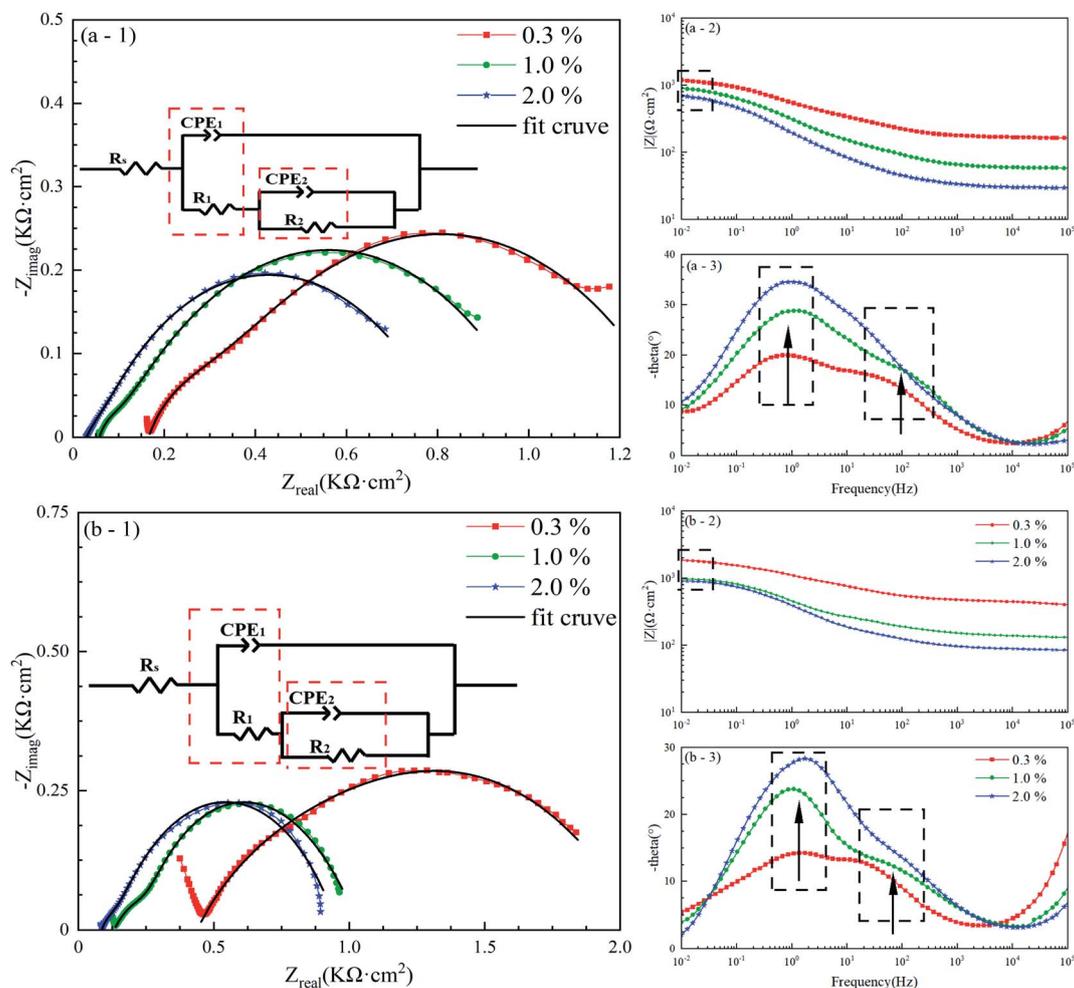

Fig. 13 Nyquist plots of X80 steel in various silty media: (a) NaCl and (b) Na_2SO_4.

Table 3 Estimated polarization resistance values

Salt	Ion concentration (%)	$R_p \approx |Z|_{0.01\ Hz}$ (Ω)	Frequency range: 10 000–0.01 Hz			$R_p = R_1 + R_2$ (Ω)
			R_s (Ω)	R_1 (Ω)	R_2 (Ω)	
Cl$^-$	0.3	1190.7	166	215.7	960.1	1175.8
	1.0	899.3	58	72.5	897.9	970.4
	2.0	697.2	29.2	175.8	622.9	798.7
SO$_4^{2-}$	0.3	1845.6	437.8	837.1	794.7	1631.8
	1.0	966.9	132.1	221.6	687.2	908.8
	2.0	894.6	86.4	111.4	759.8	871.2

Table 4 Penetration rate and mass loss rate values

Salt	Ion concentration (%)	B (mV)	$R_p \approx |Z|_{0.01\ Hz}$		$R_p = R_1 + R_2$	
			PR	MR	PR	MR
Cl$^-$	0.3	79.98	0.78	16.79	0.79	17.01
	1.0	60.79	0.79	16.90	0.73	15.66
	2.0	107.95	1.79	38.71	1.57	33.79
SO$_4^{2-}$	0.3	56.05	0.35	7.60	0.40	8.59
	1.0	30.97	0.37	8.01	0.39	8.52
	2.0	41.83	0.54	11.69	0.56	12.01

dependent on the ionic motion rate. The directed movement speed of the ions in the soil pore solution accelerated with increasing temperature, leading to enhanced ion adsorption. The strongly adsorbing ions tend to cluster in passivation film defect sites, which subsequently decrease soil oxygen content and corrosion rate, and the formation of dense corrosion deposits block delivery of ferrous ions, making the diffusion rate slower than iron oxidation. In this case, the electrode surface shows high chemical inertness, which enhances the steel resistance and prevents the corrosion process. Thus, the corrosion resistance of X80 pipeline steel could likely be improved with a higher soil temperature.

Taken together, in the corrosive soil environment at a range of concentrations used in this study, when the soil temperature is 293.15 K, as the ion concentration increases, the corrosion behavior of X80 steel samples in the chloride-containing silty soil gradually enhances drastically. The corrosion behavior of X80 steel in the sulfate-containing soil environment first decreases and then continues to increase. The corrosivity in the chloride-containing soil environment is significantly higher than that in the sulfate-induced corrosion environment.

3.1.3. Mechanism analysis. Simultaneous presence of the electrolyte (salt-containing solution) and oxidant (oxygen) in the soil is a sufficient condition for the corrosion to occur. The existence of salt ions plays a facilitating role in the cathodic reaction of steel. When salt ions present in the soil pore solution act on the interface of the metal–soil pore, local corrosion occurs. The different salts present in the soil pore solution produce diverse effects on the corrosion behavior, resulting in differences in its corrosion resistance.

When the constant soil temperature is 293.15 K, the corrosion behavior of X80 steel in silty soil containing chloride ions becomes significantly higher than that in the sulfate corrosion environment. Partly, the reason is that the chloride ions have stronger adsorption behavior. Through the adsorption–dissolution process between chloride ions and metal atoms, the corrosion can be accelerated. The adsorption of chloride ions on the metal surface is essentially a process of exchange with H$_2$O molecules. The X80 steel surface is positively charged, and the oxygen atom from lattice water molecules in the soil pore solution can get adsorbed on the metal surface atoms due to the high electronegativity of oxygen, as shown in Fig. 14(b). Nevertheless, chloride ions feature the typical physical adsorption, under the electrostatic action, they can be characteristically adsorbed on the positively charged surface, and can get preferentially adsorbed on the defects of the metal crystal surface (Fig. 14(c) and (d)). Simultaneously, chloride ions react with two adjacent metal atoms, decrease the total free energy of the metal surface, and repel the water molecules initially adsorbed on the metal surface. These effects result in competitive adsorption between water molecules and chloride ions on the metal crystal surface. The water molecules initially adsorbed near the metal atoms gradually move away from the metal surface over time.

Chloride ions interact with the electrode surface to form covalent bonds or coordination bonds. The metal atoms on the surface are attracted by the chloride ions in the soil pore solution, causing them to deviate from the original lattice positions, and then vibrate near their equilibrium positions. Concurrently, the diffusion of metal atoms is affected, resulting in disordered movement of metal ions and increase in the activity of anodic metal ions.[37] The adsorption of chloride ions similarly causes it to continue to diffuse and adsorb inward due to the attractive effect by other atoms on the crystal surface, which leads to the increase in the concentration and content of active anions inside the crystal defects. Gradually, the chloro-complex formed on the steel surface replaced the more stable oxide-ion, becoming the active site of corrosion, reducing the activation energy of the anodic dissolution process of the metal material, and eventually accelerating the corrosion rate.

The other possible reason is that the XPS results indicate that the corrosion products produced under the soil corrosion system in this test consisted mainly of FeO, FeOOH, Fe$_3$O$_4$, and other iron oxides (as shown in Fig. 14(a)). These corrosion products continue to chemically react with the strongly adsorbed chloride ions. For instance, Fe(OH)$_2$ reacts with chloride ions to release ions that can continue to participate in the
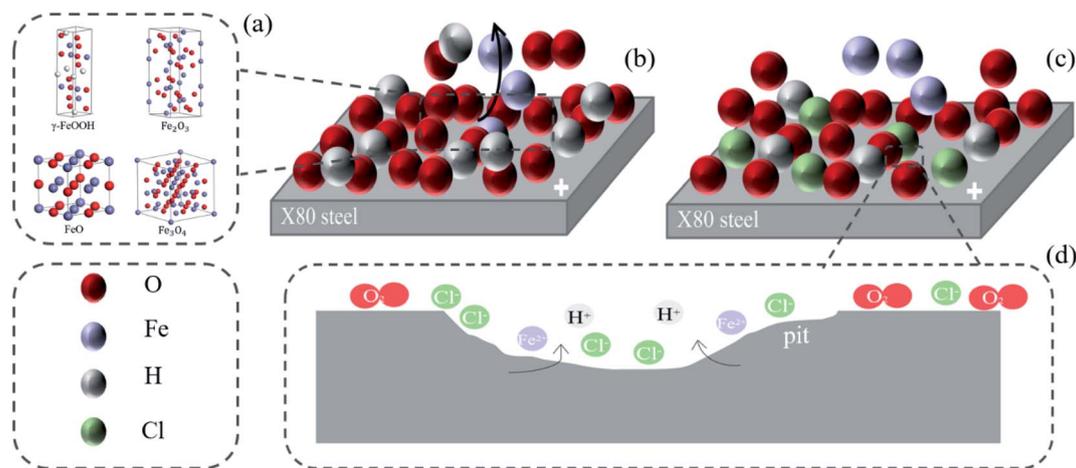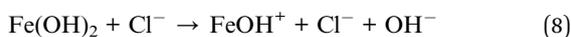
Fig. 14 Schematic representation of interface corrosion between X80 steel and chloride-containing pore solution: (a) the corrosion products, (b) the oxygen atom from lattice water molecules in the soil pore solution can get adsorbed on the metal surface atoms due to the high electronegativity of oxygen, (c) and (d) chloride ions feature the typical physical adsorption, under the electrostatic action, they can be characteristically adsorbed on the positively charged surface, and can get preferentially adsorbed on the defects of the metal crystal surface.

reaction (eqn (8)), thus increasing local electrochemical activity. Moreover, FeOOH gets dissolved by chloride ions to form a layered compound FeOCl (eqn (9)). FeOCl belongs to the orthorhombic system, showing the stack of irregular lamellae structures, and the interface of the interlayer is relatively fuzzy (as shown in Fig. 4(b)).[24,38,39]

The unstable compound FeOCl further decomposes into hydroxide anion, ferri ion, and chloride ion (eqn (10)). The presence of trivalent iron and chloride ions accelerates the corrosion process, causes corrosion under the passivation film on the metal surface, and leads to the increase in the occurrence of pitting corrosion. In summary, the kinetics behavior of X80 steel corrosion in the chloride-containing soil environment is even more dramatic.

$$Fe(OH)_2 + Cl^- \rightarrow FeOH^+ + Cl^- + OH^- \quad (8)$$

$$FeOOH + Cl^- \rightarrow FeOCl + OH^- \quad (9)$$

$$FeOCl + H_2O \rightarrow Fe^{3+} + Cl^- + 2OH^- \quad (10)$$

3.2. Corrosion behavior of X80 steel in silty soil with temperature as the independent variable

A lot more systematic explorations are further required to investigate this topic. Therefore, the soil temperature range was set from 283.15 to 263.15 K, and electrochemical tests were performed on X80 steel samples at ±5 K temperature intervals.

3.2.1. Electrochemical characterization. The stable values from the OCP monitoring of the X80 steel in silty soil with temperature as the independent variable are shown in Fig. 15. It is found that with the decrease of the soil temperature, the OCP values show an overall downward trend, and the OCP difference (Δ_{OCP}) increases first and then decreases, ranging between 0.006–0.147. The reason for minor change within a certain

range of the OCP values may be related to the microstructural properties of the steel, the physio-chemical parameters of the soil, and the soil–steel interface reaction. Therefore, subsequent electrochemical measurements are used to study the electrochemical reactions that may occur at the soil–steel interface.

The results from electrochemical measurements of the X80 steel in medium saline silty soil with temperature as the independent variable are shown in Fig. 16 and 19. During the polarization process, electrochemical, mass transport, chemical, and adsorption–desorption processes occurred on the steel surface. With the gradual positive shift of the potential and reaching the passivation potential of the material, the material primarily undergoes passivation. Next, the potential continues to increase, the passivation state of the sample steel alters, and the curve shows the feature of entering the trans-passive zone. Fig. 16 illustrates that with the decrease of soil temperature, the polarization curve shifts toward lower current, the passivation potential becomes higher, and the corrosion current density as well as passivated current density decrease. Consequently, both
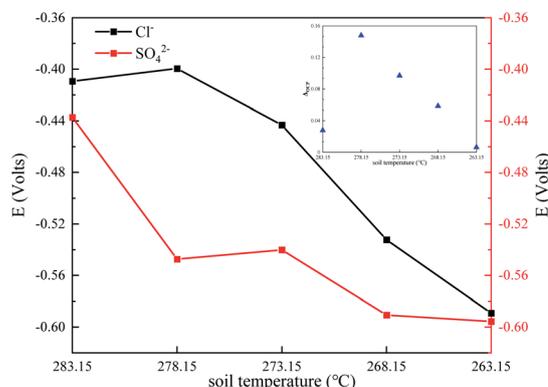

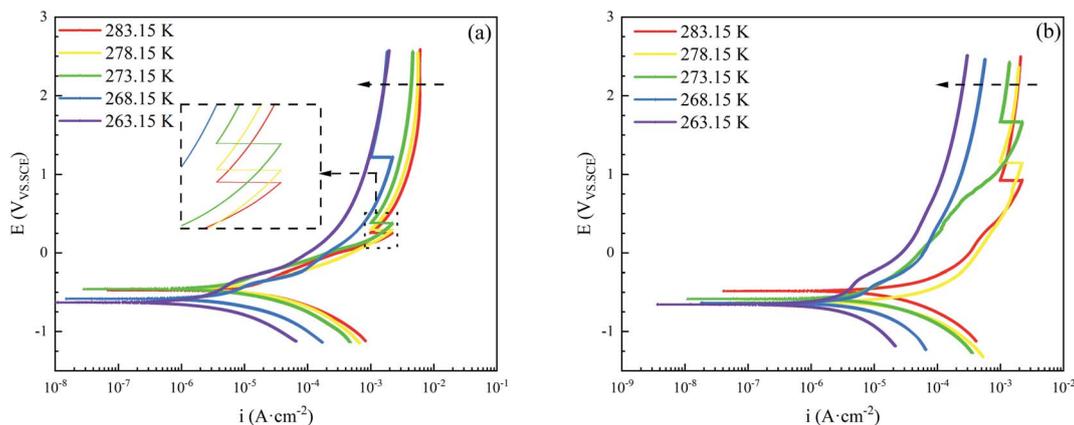**Fig. 15** Open circuit potential curves of X80 steel under different soil temperatures.

Fig. 16 Polarization curves of X80 steel under different soil temperatures: (a) NaCl and (b) Na_2SO_4.

the cathodic hydrogen evolution reaction and the anodic iron dissolution would be significantly reduced. In other words, the sample steel in the corrosive soil environment exhibits higher chemical inertness and better corrosion resistance. The corresponding corrosion parameters and surface corrosion morphologies of X80 steels are shown in Fig. 17.

In this temperature range, along with the lowering of soil temperature, the corrosion kinetic behavior of X80 sample steel in the corrosive silty soil environment also showed a decreasing tendency. In soil environments at temperatures above freezing point, the chloride-containing silty soil is more corrosive. According to the surface and microcosmic morphology of X80 steel presented in the inset of Fig. 17(c), the corrosion deposited layers composed of oxy–hydroxide compounds and hydrous ferric oxides on the surfaces have a bilayer structure at temperatures above freezing point. The outer layer is warm brown sediment, and the inner layer corresponds to a black corrosion product. The petal-like sediment layer with cracks on the surface has already reached a critical thickness when the

temperature is 283.15 K, leading to poorer layer adhesion and causing sediment to easily peel off from the surface.[40] When the temperature was decreased to 278.15 K, the surface of X80 steel was covered with looser flocculent sediments. When the temperature was 273.15 K, the corrosion rate of X80 steel in the two corrosive environments was similar, and when the soil temperature decreased to 263.15 K, the sulfate-containing silty soil was more corrosive than the chloride-containing silty soil. The decrease of unevenly distributed corrosion-induced deposits on the surface of X80 steel in sulfate-containing silty soil with decreasing temperature and a scattered trend were observed. This is attributed to the formation of ice in the porous structure of soil by the phase transition with the decrease in the soil temperature, resulting in the formation of a hypoxic microenvironment in soil–steel interface. It is known that the dissolution rate of metal is controlled by the oxygen diffusion in the soil electrolyte.[41] The dissolution rate of the metal matrix becomes lower due to the high oxygen diffusion resistance at this point.
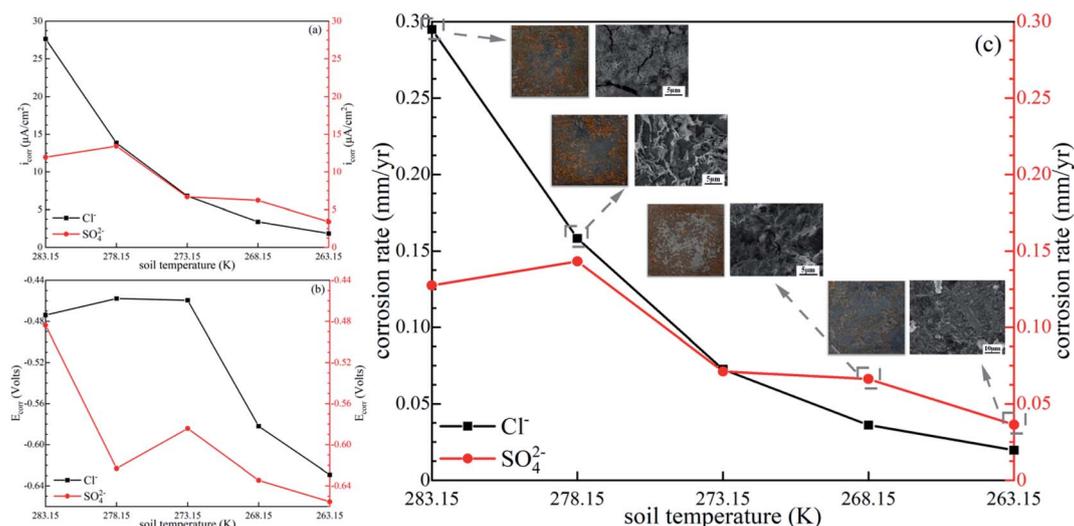

Fig. 17 Polarization curve fitting parameter value: (a) i_{corr}, (b) E_{corr}, and (c) corrosion rate.
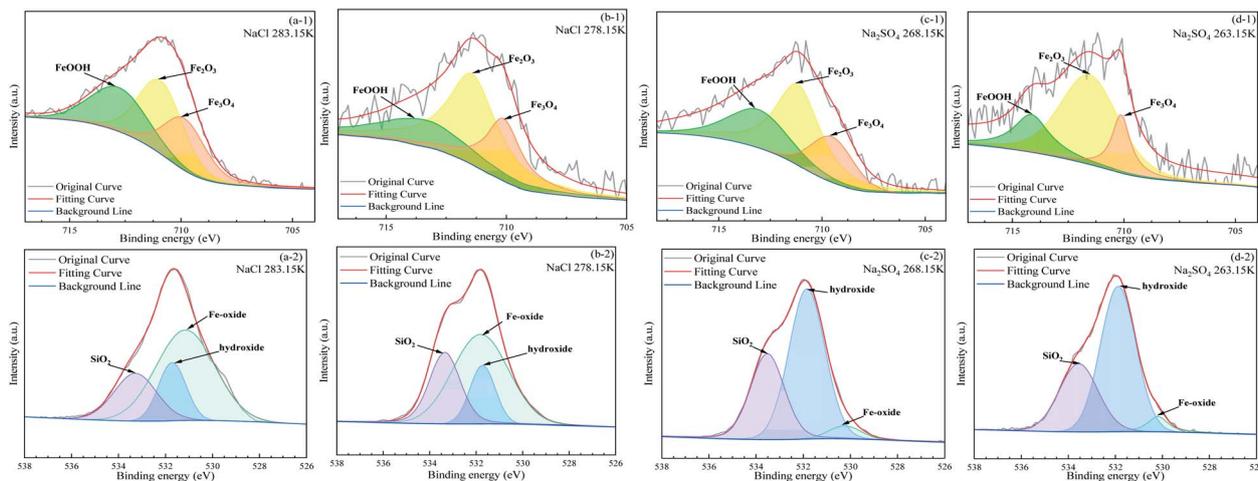
Fig. 18 High-resolution XPS spectra of Fe 2p 3/2 and O 1s of corrosion products on the steel surfaces under different soil temperatures: (1) Fe 2p 3/2, (2) O 1s, (a) 283.15 K, (b) 278.15 K, (c) 268.15 K, (d) 263.15 K.

In order to gain better insight into the difference in corrosion behavior caused by different silty soil systems, we determined the sample to be tested according to the PC test results (as shown in Fig. 17) and further supplemented the XPS characterization test of typical X80 steel interfacial corrosion deposits at different temperatures. The XPS spectra of the elements O 1s and Fe 2p 3/2 are shown in Fig. 18.

As depicted in Fig. 18, the corrosion deposits on the surface of X80 steel at different temperatures are mainly composed of iron oxides and some soil particles. Different soil temperatures have a relatively small impact on the type of corrosion deposits but greatly affect the composition and morphology of deposits. In particular, the decrease in soil temperature has an inhibitory effect on the kinetic behavior of metal corrosion that is consistent with the analysis of surface topography at macro and micro-scales results mentioned above.

The formation and transformation of corrosion deposits on the surface of X80 steel are different in different media. At temperatures above freezing point, the O 1s spectrum of X80 corrosion surface could be decomposed into three Gaussian peaks corresponding to iron oxides (O^{2-}), hydroxyl groups (OH^-) and soil particles (SiO_2), respectively.[30,31] At temperatures below freezing point, however, the O 1s spectrum could be decomposed into three peaks, which can be attributed to hydroxyl groups (OH^-), soil particles (SiO_2) and a small number of iron oxides (O^{2-}), respectively. The XPS spectra of Fe 2p 3/2 could be decomposed into three major peaks. They were assigned to FeOOH, Fe_2O_3, and Fe_3O_4, respectively.[16,42] It can be seen that the content of corrosion deposits decreases with the lowering soil temperature. At temperatures above freezing point, the Fe_2O_3 content is higher. This is because the dehydration reaction took place, and the FeOOH with poor crystal quality was converted to more stable Fe_2O_3. At temperatures below freezing point, the ice phase gradually precipitated from pore solution to the soil–steel interface, hindering the oxygen spreading depolarization. Since the relatively low concentration of iron ions flows into the soil with the decrease in soil

temperature, the degree of corrosion decreases, and the content of corrosion product formed at the soil–steel interface decreases.

The EIS results markedly changed under different situations of soil temperatures (as shown in Fig. 19). In the Nyquist plots of the X80 steels, the centers of high-frequency semicircle are positioned below the real part (*x*-axis), indicating the formation of the coarse and nonhomogeneous products layer after corrosion tests. Moreover, with the decrease in the temperature, the radii of low-frequency arc and high-frequency capacitive arc increase, and the impedance modulus at 0.01 Hz (Fig. 19(a-2) and (b-2)) as well as corrosion rate decrease. This is consistent with the PC results mentioned above. The diffusion impedance part of the low-frequency region indicates the diffusion rate of oxygen through the porous layer of corrosion product, and oxygen reduction occurs on the active metal surface at the bottom of the porous product layer. In the soil environments at temperatures below freezing point, the ice phase gradually precipitated from pore solution, and its existence resulted in the reduction of the mass-transfer efficiency of oxygen. At this time, the soil environment exhibited very poor electrical conductivity. In the phase angle diagrams (Fig. 19(a-3) and (b-3)), the change of the maximum phase angle indicates the change of the electrochemical reaction occurring on the surface of the electrode. Clearly, the maximum phase angle in the sulfate-containing silty soil undergoes a larger shift range with the decrease of soil temperature, indicating that under low temperatures below freezing point, its corrosion degree is greater than that in chloride-containing silty soil.

3.2.2. Average corrosion rate. The weight loss method is a useful measure to determine metal corrosion.[35] From the weight loss results, the average corrosion rate (ACR) of the X80 steel was determined (as shown in Table 5). The results exhibited a decrease in ACR with the decrease of soil temperature. The conductivity of silty soil at temperatures below freezing point deteriorates, the ice phase gradually precipitates from pore solution and impedes the flow of electrical current. At
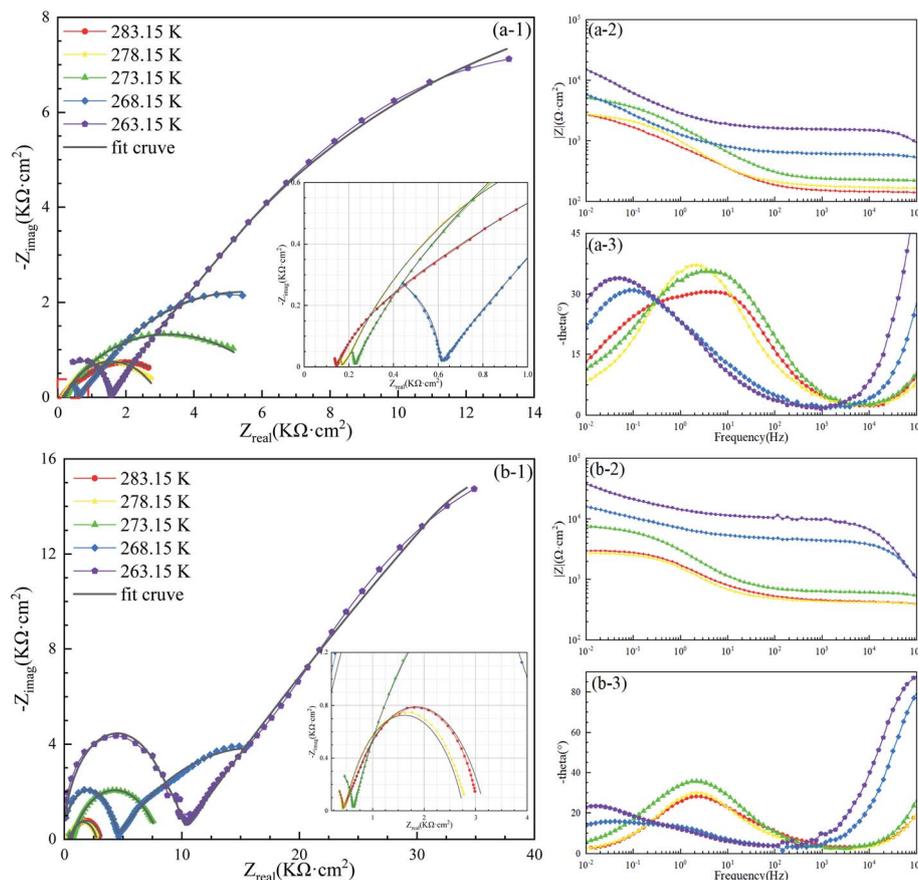
Fig. 19 Nyquist plots of X80 steel under different soil temperatures: (a) NaCl and (b) Na_2SO_4.

temperatures above freezing point, the corrosion of X80 steel in the chloride-containing silty soil is significantly stronger than that in the sulfate-containing silty soil. Nevertheless, at temperatures below freezing point, the sulfate-containing silty soil presents more corrosive, and its ACR is twice that of the chloride-containing silty soil. The trend of weight loss results is the same as the above trend of corrosion rate calculated by polarization curve, which confirms the difference in corrosion behavior caused by chloride ions and sulfate ions in silty soil at different temperatures.

3.2.3. Mechanism analysis. After the metal contacts with the soil, the soil–steel interface undergoes a complex and special corrosion process due to the non-homogeneity and

porous nature of the soil. The anodic reaction of the corrosion process indicates the anodic dissolution of metals or the formation of metal oxides and hydrous metal oxides, that is, the precipitation of dissolved metal ions and the deposition of oxides or hydroxides.

The metal ionic diffusion has a relatively significant effect on the soil corrosion process. Noteworthy, the migration processes of dissolved oxygen and iron ions affect the formation process and proportion of formed corrosion products. Fig. 20 shows the anodic iron dissolution reaction mechanism and iron ion diffusion model.[43–45] The upper and lower parts, respectively, correspond to the electrolyte environment containing sulfate ions and chloride ions. Considering the X80 steel as an example, a thinner liquid membrane on the interface is formed by soil–steel system after contact. When the dissolution of the iron anode occurred, and Fe^{2+} was formed, the difference of concentration gradient was generated, leading to gradual diffusion.[16] The soil electrolyte has a larger inherent heterogeneity; therefore, the vast majority of iron ions continued to undergo reactions to form iron oxides or oxy-hydroxide compounds attached to the steel surface, and its small fraction diffused to the pores of the soil.

The structure and particle size of the soil determine its permeability and directly affect the migration rate of the liquid and gas components present in soil.[16] The soil is a type of

Table 5 Average corrosion rate values

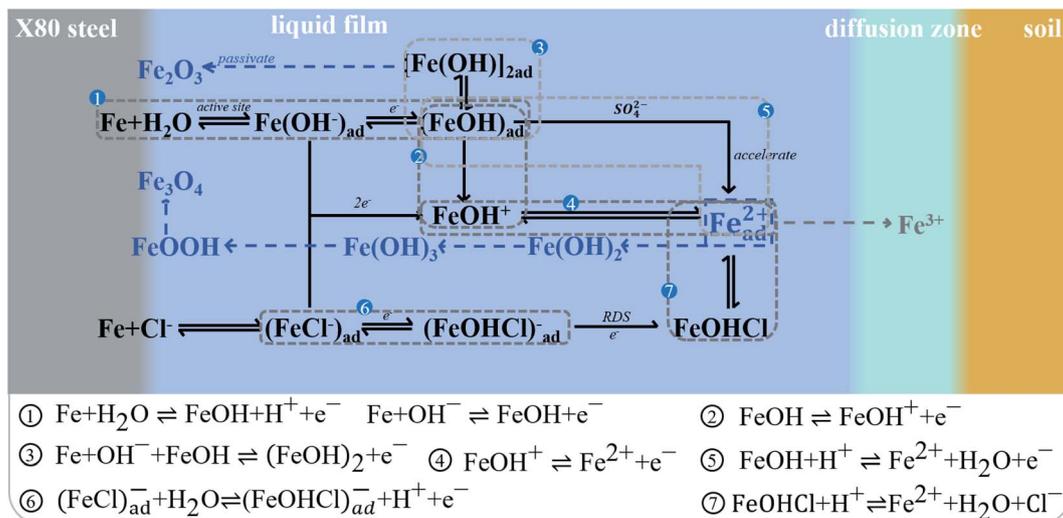| Soil temperature (K)	Cl⁻		SO₄²⁻	
	Mass loss (mg)	ACR	Mass loss (mg)	ACR
283.15	67.84	0.29	42.11	0.18
278.15	54.36	0.23	42.96	0.19
273.15	27.33	0.12	23.56	0.10
268.15	8.09	0.03	16.6	0.07
263.15	4.95	0.02	8.93	0.04

Fig. 20 Anodic dissolution reaction mechanism and iron ion diffusion models of X80 steel.

complicated system in terms of composition and property; therefore, the corrosion resistance of the metal can be improved compared with the simulated soil solution.[46,47] The composition and state of the soil pore solution near the metal surface also affect the soil corrosion process. Specifically, under aerobic conditions, the main reduced mediators that affect the corrosion behavior are pore solution and oxygen. The mass transfer process has a substantial impact on the corrosion rate. In other words, the content of the effectively reduced mediator in the electrolyte has unique control over the corrosion process.[42]

Soil corrosion at temperatures below freezing point is a complex stage controlled by the freezing process. The decrease of soil corrosiveness at temperatures below freezing point is mainly attributed to the ice phase gradually precipitating from the pore solution and leading to the blocking of electric/ionic conduction. Moreover, the oxygen content of soil pore gradually decreases, the oxygen is gradually dispersed in the pore solution further away from the crystalline plane, which leads to less adsorption on the plane, resulting in the depletion of oxidizing agent on the metal surface. In this case, mainly hydrogen ion reduction reaction occurs at the metallic cathodes to generate hydrogen atoms on the surface. However, atomic hydrogen binding to generate hydrogen requires high activation energy, leading to corrosion batteries being difficult to supply, and an adsorption film of hydrogen atom is formed on the cathode surface, thus hindering the cathodic reaction.

The corrosion degree of X80 steel in the sulfate-containing silty soil at temperatures below freezing point was significantly higher than that in the chloride-containing environment. One possible reason is that the adsorption of chloride ion becomes weaker with the decrease in the temperature. Another possible reason is that Na_2SO_4 absorbs water to form $Na_2SO_4 \cdot 10H_2O$, and the volume expansion of mirabilite decahydrate by up to about 3–4 times larger than that of $NaCl \cdot 2H_2O$ developed from NaCl.[48] With the increase in the test time and decrease in the temperature, the sulfate in the soil pore solution becomes

more amenable to the occurrence of crystallization-induced expansion. The expansion created by the hydration migration of sulfate ions leads to the bulging deformation of the soil and simultaneously generates some level of mechanical tension to affect the soil–steel interface.

The swelling deformation of the soil refers to the salt heaving and frost heaving deformation. For the sulfate-containing silty soil, the salt heaving deformation plays a determinant role. The temperature changes act as the external condition for salt-swelling deformation, and the salt concentration and water content of the soil pore solution are the internal conditions for salt-swelling deformation. Its deformation properties are affected primarily by the state of salt in the soil (the state of salt includes the salt precipitation and dissolution) and the soil structure.

With the continuous decrease of temperature, the salt-heaving deformation gradually occurs in the soil, and the deformation of the soil is cumulative and irreversible.[49] The larger the soil volume, the greater the spatial extent for deformation. Therefore, the salt heaving deformation of fine-grained soil is greater than that of coarse-grained soil. When the soil particles are mixed with the crystallized powdered sodium sulfate, the overhead structure appears, and the interparticle pores provide space for deformation due to the honeycomb-like structure of the silty soil. In parallel, larger amounts of adsorbed cations are present in sulfate-containing silty soil. They interact with neighboring colloids due to the strong hydrophilicity of cations, forming a bound water film around colloidal particles and clay particles. Thus, this leads to the reduction in the cohesion between the soil particles, separation of the soil particles, and eventually swelling deformation of soil.

When being subjected to the phase transition from water to ice, the diffusion of the solute molecules, hydrodynamic dispersion, and other physicochemical roles, the salt gets attached to the metal surface by migration, aggregation, and precipitation. The adsorbed ions exhibit certain electrical

conductivity. Thus, the place where the salt ions adhere to the surface becomes the corrosion active site again, forming localized corrosion cells on the metal surface, accelerating metal dissolution, and promoting the formation of pitting-type corrosion.

4. Conclusions

This study offers a comprehensive and objective analysis of the synergistic effect of salt and temperature in the silty soil system on the corrosion impact of API 5L X80 pipeline steel. The following major findings emerged from this study:

(1) At 293.15 K, the loose-surface deposited layer of X80 steel in the sulfate-containing silty soil contains more reduced state substances and grows perpendicular to the surface, the layer is mostly distributed in a fluffy cluster, and the degree of corrosion is relatively mild. For the X80 steel present in the chloride-containing silty soil, the deposited layer contains more oxidation state substances and grows along the steel surface, which easily promotes the occurrence of under-deposition corrosion.

(2) The impedance spectroscopy is used to determine the polarization resistance. In turn, it is concluded that the variation tendency of penetration rate and mass loss rate of X80 steel in various silty soil media is the same as that of the corrosion rate calculated by using the polarization curve. Therefore, it represents a plausible way to extract information regarding the corrosion of the specimen based on the impedance spectroscopy data.

(3) The corrosion kinetic analysis shows that the different ions in the silty soil pore solution cause differences in the corrosion behavior of X80 steel at different soil temperatures. At temperatures above freezing point, due to the adsorption-dissolution process between chloride ions and metal atoms and with continuous occurrence of the chemical reaction with corrosion products, the corrosion of X80 steel in the chloride-containing silty soil is significantly stronger than that in the sulfate-containing silty soil.

(4) At temperatures below freezing point, soil corrosion is a complex stage controlled by the freezing process. The sulfate in the soil pore solution is more amenable to the occurrence of crystallization-induced expansion. The expansion of sulfate ions leads to the bulging deformation of the soil body and simultaneously generates some level of mechanical tension to affect the soil–steel interface, resulting in more corrosion of the X80 steel in a sulfate corrosion environment.

Conflicts of interest

There are no conflicts to declare.

Acknowledgements

References

1 *BP Statistical Review of World Energy*, 2021, https://www.bp.com/, accessed Sep 2021.

2 *The Impacts of the COVID-19 Crisis on Global Energy Demand and CO2 Emissions*, https://www.weforum.org/, accessed Sep 2021.

3 A. T. Hoang, N. Sandro, A. I. Olcer, H. C. Ong, W. H. Chen, C. T. Chong, S. Thomas, S. A. Bandh and X. P. Nguyen, *Energy Policy*, 2021, **154**, 112322.

4 Y. Du, X. Yin, J. Lai, Z. Ullah, Z. Wang and J. Hu, *Int. J. Electr. Power Energy Syst.*, 2021, **133**, 107110.

5 D. W. Kim, S. S. Sohn, W. K. Kim, K. S. Kim and S. Lee, *Sci. Rep.*, 2018, **8**, 15598.

6 Y. Shuai, X. H. Wang and Y. F. Cheng, *J. Nat. Gas Sci. Eng.*, 2021, **93**, 104016.

7 X. Zhou, T. Wu, L. Tan, J. Deng, C. Li and W. Qiu, *J. Mater. Res. Technol.*, 2021, **12**, 2224–2237.

8 C. Liu, Z. Li, B. Zhao, Z. Liu, C. Du and X. Li, *J. Mater. Res. Technol.*, 2021, **14**, 533–547.

9 T. Wang, D. Xu, L. Qu, J. Fu and Z. Li, *Int. J. Pressure Vessels Piping*, 2021, **192**, 104413.

10 Z. Zhang, X. Ni and Y. Frank Cheng, *Constr. Build. Mater.*, 2020, **260**, 120459.

11 Y. Shuai, X. H. Wang, J. Li, J. Q. Wang, T. T. Wang, J. Y. Han and Y. F. Cheng, *Ocean Eng.*, 2021, **234**, 109228.

12 Y. Hou, Q. Fang, D. Zhang and L. N. Y. Wong, *Tunn. Undergr. Space Technol.*, 2015, **46**, 76–84.

13 Y. Huang, D. Xu, L. Y. Huang, Y. T. Lou, J. B. Muhadesi, H. C. Qian, E. Z. Zhou, B. J. Wang, X. T. Li, Z. Jiang, S. J. Liu, D. W. Zhang and C. Y. Jiang, *npj Biofilms Microbiomes*, 2021, **7**, 6.

14 R. Hirata, A. Ooi, E. Tada and A. Nishikata, *Corros. Sci.*, 2021, **189**, 109568.

15 Q. Qin, J. Xu, B. Wei, Q. Fu, L. Gao, C. Yu, C. Sun and Z. Wang, *Bioelectrochemistry*, 2021, **142**, 107911.

16 Z. Bai, K. Xiao, P. Dong, C. Dong, D. Wei and X. Li, *RSC Adv.*, 2018, **8**, 40544–40553.

17 H. Ma, B. Zhao, Z. Liu, C. Du and B. Shou, *Constr. Build. Mater.*, 2020, **243**, 118203.

18 M. A. Tabatabai, A. I. Payne, J. R. Freney and R. H. Miller, *Methods of Soil Analysis*, Soil Science Society of Ameriea, Madison, Wisconsin, 1982.

19 D. Yang, C. Yan, J. Zhang, S. Liu and J. Li, *Constr. Build. Mater.*, 2021, **267**, 120979.

20 X. Wan, E. Liu, E. Qiu, M. Qu, X. Zhao and F. J. Nkiegaing, *Cold Reg. Sci. Technol.*, 2020, **172**, 102988.

21 M. Zhu, Y. M. Wang, Y. F. Yuan, S. M. Yin and S. Y. Guo, *Trans. Mater. Heat Treat.*, 2019, **40**, 98–106, in Chinese.

22 S. Zhang, J. Liu, M. Tang, X. Zhang and K. Wu, *J. Mater. Res. Technol.*, 2021, **11**, 519–534.

23 L. M. Zhang, M. C. Yan, S. D. Zhang, L. Y. Zhu, A. J. Umoh, A. L. Ma, Y. G. Zheng and J. Q. Wang, *Corros. Sci.*, 2020, **164**, 108305.

24 Z. Mahidashti, M. Rezaei and M. P. Asfia, *Colloids Surf., A*, 2020, **602**, 125120.

25 O. M. A. Khamaysa, I. Selatnia, H. Lgaz, A. Sid, H.-S. Lee, H. Zeghache, M. Benahmed, I. H. Ali and P. Mosset, *Colloids Surf., A*, 2021, **626**, 127047.

26 E. Huape-Padilla, L. Béjar-Gómez, M. Sanchez-Carrillo, A. Medina-Flores, H. G. Carreón-Garcidueñas, S. E. Borjas-García and R. Huirache-Acuňa, *Microsc. Microanal.*, 2018, **24**, 1086–1087.

27 Q. Fu, J. Xu, B. Wei, Q. Qin, L. Gao, Y. Bai, C. Yu and C. Sun, *Int. J. Pressure Vessels Piping*, 2021, **190**, 104313.

28 L. A. de Oliveira, O. V. Correa, D. J. dos Santos, A. A. Z. Páez, M. C. L. de Oliveira and R. A. Antunes, *Corros. Sci.*, 2018, **139**, 21–34.

29 W. Zhang, H. J. Li, M. Wang, L. J. Wang, Q. Pan, X. Ji, Y. Qin and Y. C. Wu, *J. Mol. Liq.*, 2019, **293**, 111478.

30 R. Z. Qin, Y. X. Du, Z. C. Xu and M. X. Lu, *Materials*, 2019, **3**, 394.

31 R. Z. Qin, Y. X. Du, Z. C. Xu and M. X. Lu, *RSC Adv.*, 2019, **9**, 7698–7774.

32 Y. Korobov, H. Alwan, N. Soboleva, A. Makarov, N. Lezhnin, V. Shumyakov, M. Antonov and M. Deviatiarov, *J. Therm. Spray Technol.*, 2021, 1–13.

33 ASTM G102, *J. ASTM Int.*, 2015, **89**, 1–7.

34 S. Keßler and A. A. Sagüés, *Mater. Corros.*, 2020, **71**, 849–856.

35 Y. P. Sun, C. T. Yang, C. G. Yang, D. K. Xu, Q. Li, L. Yin, C. S. Qiu, D. liu and K. Yang, *Acta Metall. Sin.*, 2019, **32**, 1483–1489.

36 B. Rosborg, T. Kosec, A. Kranjc, J. Pan and A. Legat, *Electrochim. Acta*, 2011, **56**, 7862–7870.

37 K. Shi, L. Feng, L. Yao, W. W. Li, S. B. Wang and X. F. Xie, *J. Chem. Eng. Chin. Univ.*, 2019, **33**, 843–848, in Chinese.

38 Y. Cao, K. P. Cui, Y. H. Chen, M. S. Cui, G. H. Li, D. Li and X. J. Yang, *Solid State Sci.*, 2021, **113**, 106548.

39 X. Liu, W. Y. Zhang, L. Q. Mao, Y. Yin and L. C. Hu, *J. Mater. Sci.*, 2021, **56**, 6704–6718.

40 L. S. Yang and C. Yang, *Pet. Sci.*, 2020, **18**, 285–294.

41 S. Choudhary, A. Garg and K. Mondal, *J. Mater. Eng. Perform.*, 2016, **25**, 2969–2976.

42 B. Wei, J. Xu, Q. Fu, Q. Qin, Y. Bai, C. Sun, C. Wang, Z. Wang and W. Ke, *J. Mater. Sci. Technol.*, 2021, **87**, 1–17.

43 L. C. Shui, *Corrosion electrochemistry and its measurement method*, Science Press, 2018.

44 T. Tsuru, *Mater. Sci. Eng.*, 1991, **146**, 1–14.

45 S. Haruyama, *Proc. 2nd Jpn.U.S.S.R. Corrosion Seminar*, Japan Society of Corrosion Engineering, Tokyo, 1980.

46 K. Wang, F. B. Varela and M. Y. Tan, *Corros. Sci.*, 2019, **152**, 218–225.

47 Z. Zhou, T. Wu, M. Liu, B. Wang, C. Li and F. Yin, *Int. J. Pressure Vessels Piping*, 2021, **192**, 104395.

48 Z. H. Fang, *Phys. B*, 2005, **357**, 433–438.

49 X. X. Li, S. J. Wang, R. H. Xiao, D. X. Cheng and F. Z. Yan, *Chin. J. Geotech. Eng.*, 2016, **38**, 2069–2077, in Chinese.